Journal of Biomechanics 83 (2019) 34–42

Contents lists available at ScienceDirect

Journal of Biomechanics

journal homepage: www.elsevier.com/locate/jbiomech
www.JBiomech.com

Mechanics of linear microcracking in trabecular bone

Max A. Hammond [a], Joseph M. Wallace [b], Matthew R. Allen [b,c], Thomas Siegmund [a,*]

[a] Department of Mechanical Engineering, Purdue University, West Lafayette, IN, USA
[b] Department of Biomedical Engineering, Indiana University-Purdue University at Indianapolis, IN, USA
[c] Department of Anatomy and Cell Biology, Indiana University School of Medicine, IN, USA

ARTICLE INFO

Article history:
Accepted 9 November 2018

Keywords:
Trabecular bone
Anisotropy
Heterogeneity
Stress analysis
Microcracking
XFEM

ABSTRACT

Microcracking in trabecular bone is responsible both for the mechanical degradation and remodeling of the trabecular bone tissue. Recent results on trabecular bone mechanics have demonstrated that bone tissue microarchitecture, tissue elastic heterogeneity and tissue-level mechanical anisotropy all should be considered to obtain detailed information on the mechanical stress state. The present study investigated the influence of tissue microarchitecture, tissue heterogeneity in elasticity and material separation properties and tissue-level anisotropy on the microcrack formation process. Microscale bone models were executed with the extended finite element method. It was demonstrated that anisotropy and heterogeneity of the bone tissue contribute significantly to bone tissue toughness and the resistance of trabecular bone to microcrack formation. The compressive strain to microcrack initiation was computed to increase by a factor of four from an assumed homogeneous isotropic tissue to an assumed anisotropic heterogeneous tissue.

1. Introduction

Microcracks form in vivo are considered central to the understanding of bone mechanical degradation (Frost, 1960; Wenzel et al., 1996; Verborgt et al., 2000; Acevedo et al., 2018). Images of 2D and 3D (Lambers et al., 2013) histological sections, scanning electron microscopy (Thurner et al., 2007), contrast enhanced micro-computed tomography (μCT) imaging (Wang et al., 2007) and synchrotron imaging (Larrue et al., 2011) reveal the prominence of the linear microcrack configuration. A single trabeculae containing a linear microcrack is depicted in Fig. 1A in a basic Fuchsin stained histological section under fluorescent light and in Fig. 1B through a μCT scan of bone stained with $BaSO_4$. The crack surfaces of linear microcracks in trabecular bone are shown to be predominantly aligned with the local trabecular bone surface. Fig. 1C depicts a μCT scan image of a bone core with linear microcracks broadly distributed throughout.

Relationships between microcrack parameters, mechanical loading and bone biological conditions have been established (Mori et al., 1997; Allen and Burr, 2007; Lambers et al., 2013). Crack growth in bone tissue is known to be linked to hierarchical deformation and damage mechanisms. At the length scale of individual trabeculae, crack bridging mechanisms play a key role (Yeni and Fyhrie, 2003; Thurner et al., 2007; Launey et al., 2010; Ritchie, 2010). At that scales of bone tissue can be considered as a quasi-brittle solid (Ridha and Thurner, 2013) where a nonlinear deformation response is due to damage, i.e. microcrack formation and growth. Processes leading to microcrack formation are not fully understood. One finding relates microcrack formation in trabecular bone to mechanical strains (Goff et al. 2015a, b), but another study finds no clear evidence for such a relationship (Tassani et al., 2018). Recent data have described the influence of tissue heterogeneity on microcracking in trabecular bone (Torres et al., 2016). However, the effects of combined heterogeneity and anisotropy on microcracking in trabecular bone are not known.

Computations leading to discrete microcrack formation can be conducted within the framework of cohesive material separation, either using a cohesive element formulation (Elices et al., 2002) or the extended finite element method (XFEM) (Sukumar et al., 2015). These approaches have been used in investigations of crack initiation and propagation in bone across length scales: in (Siegmund et al., 2008) in a study of the nanoscale mineralized collagen fibril, in (Hamed and Jasiuk, 2013) to microscale lamellar bone and in (Abdel-Wahab et al., 2012; Besdo and Vashishth, 2012; Feerick et al., 2013) to mesoscale cortical bone. Tomar (2008) applied the cohesive modeling technique in a 2D model of microcrack formation in trabecular bone under dynamic loading.

* Corresponding author at: School of Mechanical Engineering, Purdue University, 585 Purdue Mall, West Lafayette, IN 47907, USA.
E-mail address: siegmund@purdue.edu (T. Siegmund).

https://doi.org/10.1016/j.jbiomech.2018.11.018
0021-9290/

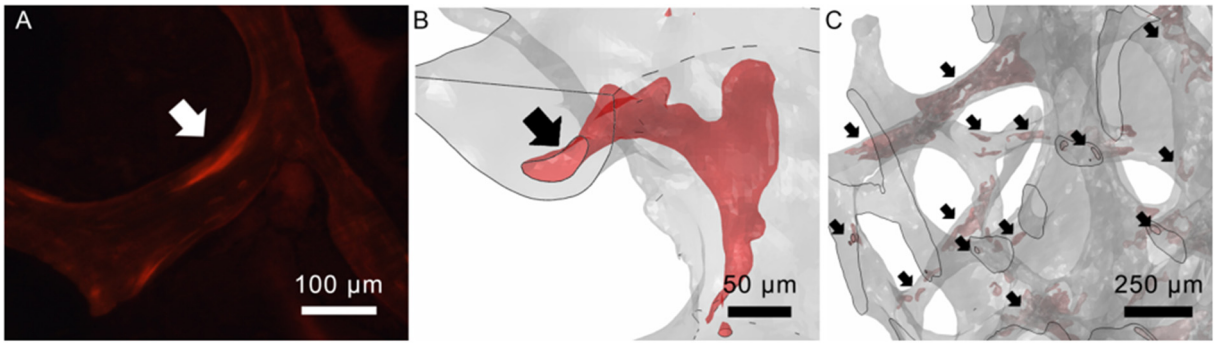

Fig. 1. Linear microcracks in trabecular bone often follow the geometry of the trabecular surface (A) Micrograph of a linear microcrack (arrow) stained using basic Fuchsin; (B) μCT visualization of a microcrack (arrow) within a trabecula stained using $BaSO_4$; (C) μCT visualization of the microcrack (arrows) spatial distribution in a trabecular bone core stained using $BaSO_4$.

Here, a XFEM approach is applied in 3D to allow for largely mesh-independent simulation of microcracking.

We hypothesized that the processes of microcrack formation and tissue resistance against microcracking are intrinsically related to the heterogeneity and anisotropy of the deformation and separation response of the tissue. Hammond et al., 2018 demonstrated that tissue heterogeneity and anisotropy have significant influence on the stress state in trabecular bone. Therefore, the hypothesis is tested by comparing the outcomes of finite element simulations of microcrack formation under four different combinations of tissue biomechanical properties varying tissue heterogeneity and anisotropy.

2. Materials and methods

2.1. Sample and model preparation

A trabecular core was obtained from the distal femur of a human cadaver (Indiana University School of Medicine Anatomical Education Donor Program). The trabecular core was imaged with a Skyscan 1172 μCT system, isotropic voxel size of 5.88 μm (Bruker μCT, Kontich, Belgium). Voxels were reconstructed with attenuation coefficients in the 0–0.11 mm^{-1} range (NRecon, Bruker μCT). Images were vertically align with Dataviewer (Bruker μCT). The sample possessed bone volume fraction of 18.2%. The average trabecular thickness was 68.3 μm. Manufacturer supplied hydroxyapatite phantoms (250 and 750 kg/m^3) were used to calibrate the mineral density (ρ) for each image grayscale (GS) value. The relationship $\rho_{GS} = 11.1\ kg/m^3 \times GS - 255\ kg/m^3$, derived from a linear fit of the grayscales of the phantoms, was used to assign tissue density values to each element of the model. Density values ranged between $\min(\rho_{GS}) = 777.3\ kg/m^3$ and $\max(\rho_{GS}) = 1576.5\ kg/m^3$ with an average value density $\text{avg}(\rho_{GS}) = 1168\ kg/m^3$.

Collagen lamellae are known to be aligned with the local surface (Reznikov et al., 2015; Georgiadis et al., 2016). The anisotropy of the tissue is defined by computing the local normal (i) to the tissue surface (j, k) (Hammond et al., 2018).

Two regions of interest were selected (CTAn, Bruker μCT) from the center of the trabecular compartment: (1) a domain (280 μm × 275 μm × 223 μm) containing a single rod-like trabecula (L_{trab} = 160 μm trabecular length, 90 μm minimum trabecular thickness), (2) a cube bone core (side length H_{core} = 3000 μm). Gaussian smoothing was applied to the regions of interest. The optimal threshold to separate bone from marrow was based on the Otsu method. A free continuum finite element mesh was created with local grayscales assigned (ScanIP (Simpleware, Montainview, CA).

For the single trabeculae model, Fig. 2A, the finite element mesh consisted of 72,614 fully integrated 10 node tetrahedral elements. At the smallest cross section there are 25 elements across the section. For the bone core model, Fig. 2B, the finite element mesh consisted of 2,544,945 such elements. For the smallest trabeculae, there are at least 4 or 5 elements across the section.

2.2. Tissue biomechanical properties

The trabecular bone tissue was a linear elastic solid with microcracks nucleating and growing. Simulations of elastic deformation, microcrack initiation and microcrack growth considered a nonlinear, large displacement finite element method with enriched elements (XFEM) with multisite microcracking (ABAQUS/Standard v2017, Dassault Systèmes SIMULIA, Johnston, RI).

Four models were created for both single trabeculae and bone core, Fig. 3. Tissue elastic and failure properties are allocated with spatial heterogeneity and anisotropy. In anisotropic models, transversely isotropic elastic properties were: $2E_i = E_j = E_k$, $\nu_{jk} = 1.25\text{-}\nu_{ji} = 0.37$, $G_{jk} = 1.5G_{ji}$. Ratios between moduli are similar to those observed experimentally (Reisinger et al., 2011). Isotropic models had values of E, ν, G equal E_j, ν_{jk}, G_{jk}. In heterogeneous models, E_i and E were adjusted based on a scaling factor derived from the ratio of the modulus calculated using the average local density within each element and the modulus calculated using the global average density in the model. The relationship $E/E_0 = (0.912\ m^2/s^2 \times \rho_{GS} - 66.2)$ (Rho et al., 1995) converts each local density value to the respective normalized local isotropic modulus. Heterogeneity did not alter ν_{jk} or ν, but varying E_i or E dictated the effect of heterogeneity on G_{jk} or G, respectively.

Two microcrack formation criteria are considered. In isotropic tissue models, microcracks initiate if the ratio of maximum tensile principal stress $\sigma_{p,\max}$ to microcrack ignition strength $\sigma_{\max}$ fulfilled the criterion $f = 1$:

$$f = \left\{\frac{\langle\sigma_{p,\max}\rangle}{\sigma_{\max}}\right\}, \quad \langle\sigma_{p,\max}\rangle = \begin{cases} \sigma_{p,\max}, \sigma_{p,\max} > 0 \\ 0, \sigma_{p,\max} < 0 \end{cases} \tag{1}$$

Microcracks are then formed in a plane normal to the maximum principal stress direction computed from the local stress state. In anisotropic tissue models, microcracks initiate if the maximum nominal stress criterion is fulfilled $f = 1$:

$$f = \max\left\{\frac{\langle t_i\rangle}{\sigma_{\max}}, \frac{t_j}{\sigma_{\max}}, \frac{t_k}{\sigma_{\max}}\right\}, \quad \langle t_i\rangle = \begin{cases} t_i, t_i > 0 \\ 0, t_i < 0 \end{cases} \tag{2}$$

The normal traction in the direction of the trabecular surface outward normal (i) is t_i. The respective shear tractions are t_j and t_k. The microcrack initiation strength was related to the local

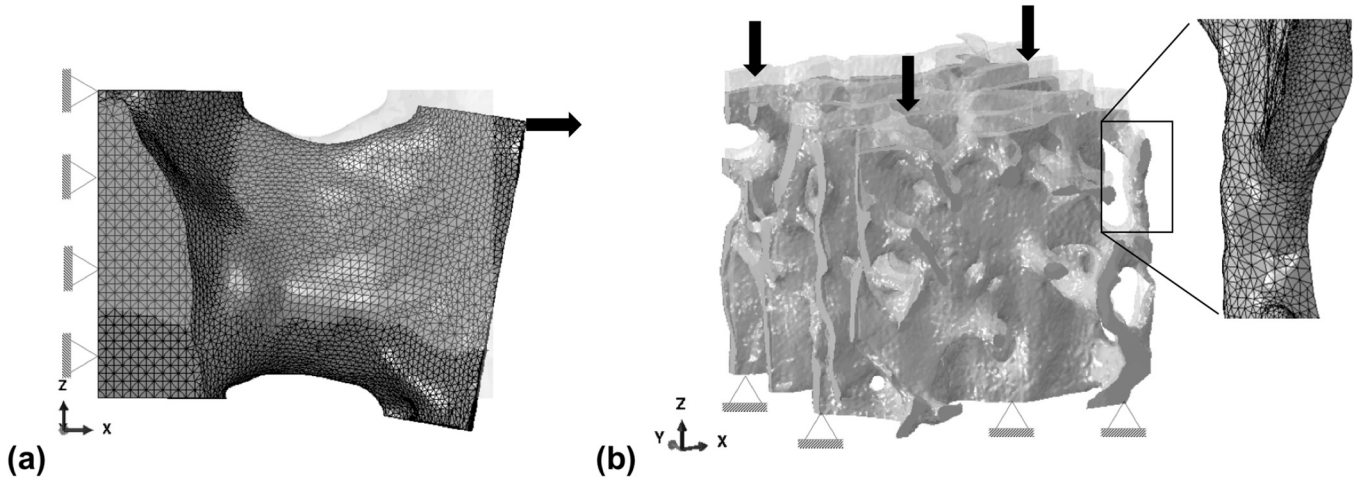

Fig. 2. Analysis models and schematic of boundary conditions: (a) single trabecula model, (b) core model with insert showing the finite element mesh.

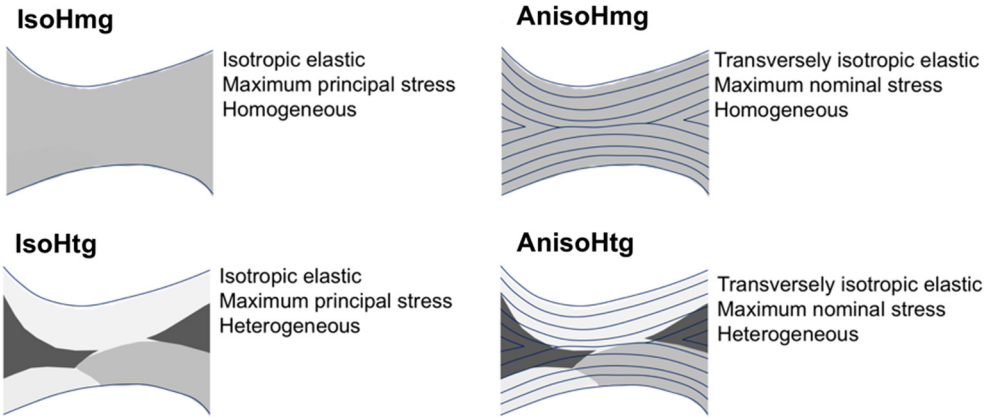

Fig. 3. Model cases considered: (a) Model case IsoHmg: the bone tissue is considered as elastic isotropic, failing following the maximum principal stress criterion and as homogeneous; (b) Model case IsoHtg: the bone tissue is considered as elastic isotropic, failing following the maximum principal stress criterion and as heterogeneous; (c) Model case AnisoHmg: the bone tissue is considered as elastic transversely isotropic, failing following the maximum nominal stress criterion with direction imposed by the fibril orientation and as homogeneous; (d) Model case AnisoHtg: the bone tissue is considered as elastic transversely isotropic, failing following the maximum nominal stress criterion with direction imposed by the fibril orientation and as heterogeneous. In the schematic drawings gray scales indicate domains of constant tissue density and lines indicate fibril orientation.

elastic modulus and a respective reference strain ε_0. In isotropic models $\varepsilon_0 = \sigma_{max}/E = (1/500)$ and in anisotropic models $\varepsilon_0 = \sigma_{max}/E_i = (1/500)$. Once a microcrack initiation criterion is fulfilled, the tractions across the microcrack decline linearly until a critical separation δ_c is reached where traction vanish. The microcrack toughness is $G_c = (1/2)\sigma_{max}.\delta_c = 0.5$ MPa mm. This value is constant in all cases. In heterogeneous models, both the modulus and strength increase from near surface domains the interior domains. At the same time the value of δ_c declines from the trabecular surface into the trabecular interior. Near surface domains are less brittle (low strength and slow decline in traction with microcrack opening) while the trabecular interior is more brittle (high strength and rapid decline the traction with microcrack opening). Friction between microcrack surfaces is neglected. Following (Lu et al., 1994) this should have minor influence on the energy release rates at the microcrack tips.

2.3. Analysis

Fig. 2 depicts the two models, including the displacement boundary conditions and details of the FE mesh. The single trabeculae was loaded under an applied eccentric displacement U_{appl} with applied strain $\varepsilon_{appl} = U_{appl}/L_{trab}$. The bone core model was loaded under an applied compressive displacement U_{appl} along the transaxial with $\varepsilon_{appl} = U_{appl}/H_{core}$. Computations were terminated once convergence became exceedingly costly.

For elements for which $f = 1$ the signed distance function from each node to the microcrack plane, the displacement of each node and the energy dissipation due to microcracking was recorded. Stress and strain values were extrapolated to the crack tip to determine if the damage initiation criterion is satisfied and to determine the crack propagation direction. The location of the microcrack plane within each element was calculated from the initial coordinates of each node, the nodal displacements and the signed distance function to the microcrack plane. Subsequently, the microcrack area for each individual element with $f = 1$ is obtained. Each element was separated into its respective microcrack region allowing the total number of microcracks and individual microcrack areas to be determined. The total microcrack area and total energy dissipation due to microcracking were obtained (MATLAB R2018a, Mathworks, Nantick, MA). Regions near the applied boundary conditions were excluded from the analysis (within 20 μm of the applied boundary conditions for the single trabeculae model and 200 μm for the core model).

3. Results

3.1. Microcracking in the single trabecula model

For single trabecula models, both IsoHmg and IsoHtg models resulted in the formation of transverse cracks at the site of minimal trabecular thickness, Fig. 4A-B. The microcrack initiated at the trabecular surface and propagated towards the interior. In AnisoHmg and AnsioHtg models, the microcrack was contained within the interior of the trabecula with the crack surface parallel to the trabecula surface, Fig. 4C-D. Heterogeneity altered the site of microcrack initiation and subsequent growth for anisotropic models. For the AnisoHmg model the microcrack was located deep into the trabecula interior (18 μm from the surface). For the AnisoHtg model the microcrack was close to the trabecula surface (3.3 μm from the surface).

Fig. 5A depicts the computed evolution of the microcrack relative to normalized applied strain $\varepsilon_{appl}/\varepsilon_0$. The transverse microcracks in the IsoHmg and IsoHtg models initiated at small values of $\varepsilon_{appl}/\varepsilon_0$ and subsequently grew rapidly. Anisotropy was found to strongly delay microcrack initiation. The value of $\varepsilon_{appl}/\varepsilon_0$ at microcrack initiation for the AnisoHmg model was 7.5 times that for the IsoHmg model and for the AnisoHtg model 3 times that of the IsoHtg model, Fig. 5A. While heterogeneity did not affect microcrack initiation for isotropic models, its effect in anisotropic models was notable. For the AnisoHtg model, microcrack growth occurred much earlier than in the AnisoHmg model, but the subsequent crack growth was negligible up to the crack initiation of the AnsioHtg model. In isotropic models the predicted microcrack growth rate was high instantaneously, a feature of brittle failure. In anisotropic models, the predicted growth rate following initiation was low and only later increased, a feature of a damage tolerant system. The energy dissipated per microcrack area was found to depend on combined effects of anisotropy and heterogeneity. At a microcrack area of 0.0015 mm^2, there was over a 3 fold higher energy dissipation predicted for the AnisoHtg case compared to the AnisoHmg case. This finding indicates a substantive difference in the progression of material separation in the period beyond microcrack initiation. On the other hand, the effect of heterogeneity in the isotropic models was minimal, Fig. 5B.

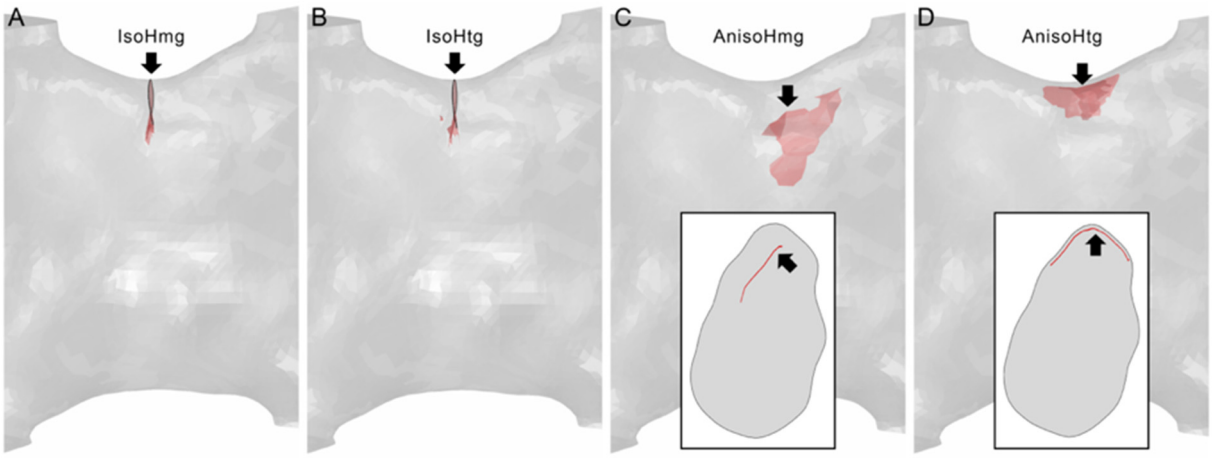

Fig. 4. Predicted microcrack morphology, single trabecula models with microcrack area 0.0015 mm^2: (A) IsoHmg model and (B) IsoHtg model: microcrack initiating (arrow) at the surface and propagating through the trabecular thickness; (C) AnisoHmg model: microcrack initiating (arrow) within the trabecula and with microcrack surface mostly parallel to the trabecular surface; (D) AnisoHtg model: microcrack initiating (arrow) in the interior and a microcrack surface following the trabecular surface. Insets in (C) and (D) depict cross-sections of the trabecula demonstrating a linear microcrack morphology and location.

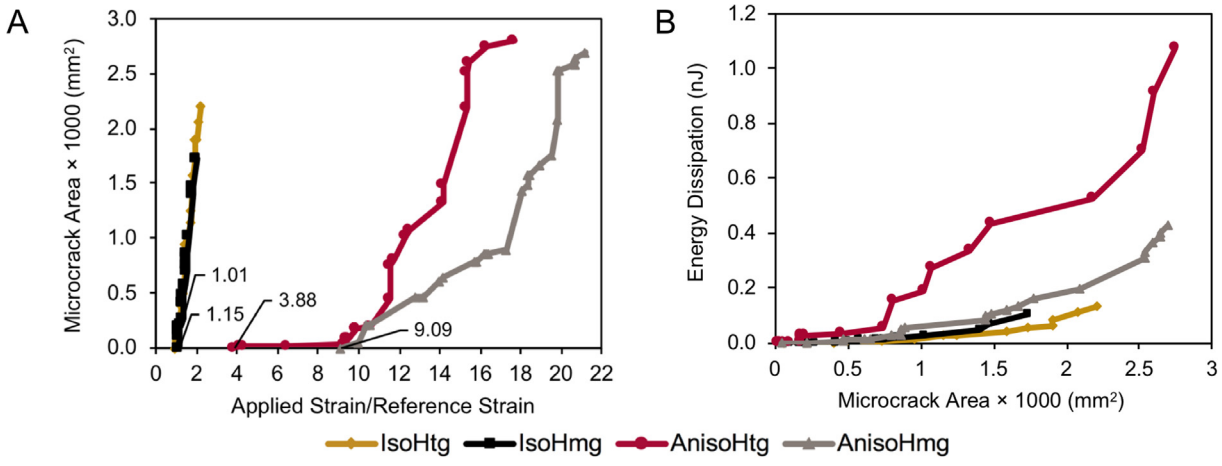

Fig. 5. Single trabecula model: (A) Microcrack area vs. normalized applied strain (strain values at initiation provided): Anisotropy increased the strain at microcrack initiation and delayed microcrack growth in homogeneous and heterogeneous models compared to the isotropic cases while heterogeneity only had a noticeable effect in the anisotropic model; (B) Energy dissipation vs. microcrack area: The interaction between anisotropy and heterogeneity produced a large increase in the energy dissipation per microcrack area in the AnisoHtg model.

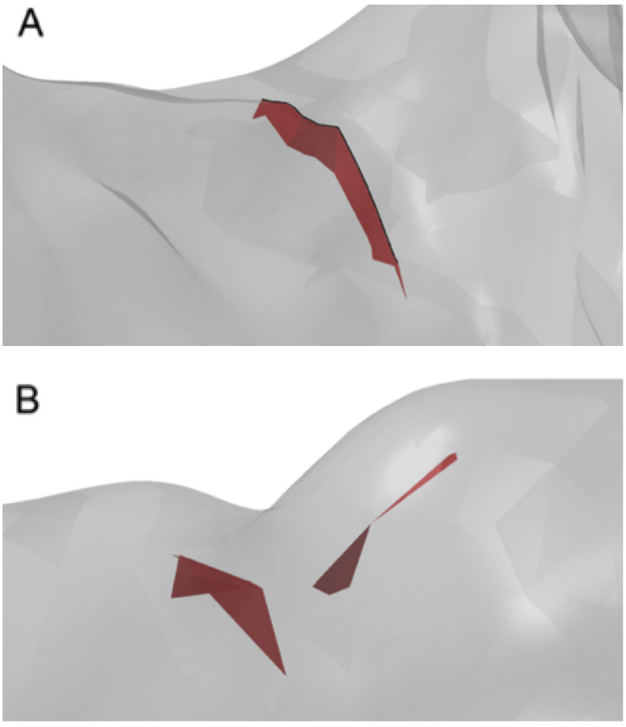

Fig. 6. Predicted microcrack morphology in the bone core models: (A) IsoHmg model: transverse microcracks originating from the surface (black line) and propagating into the depth of the trabecula; (B) AnisoHmg model: linear microcracks were predicted.

3.2. Microcracking in the bone core model

Examples of predicted microcracks in the bone core models are depicted in Fig. 6. For the IsoHmg model, Fig. 6A, transverse microcracks are formed, consistent with the single trabecula model, Fig. 4A-B. For the AnisoHmg model, Fig. 6B, microcracks following the trabecular surface are formed, consistent with the single trabecula model, Fig. 4C-D.

Fig. 7A depicts the cumulative microcrack area in dependence of $\varepsilon_{appl}/\varepsilon_0$ for the bone core models and all four tissue biomechanical models. Values for the applied strain at crack initiation ($\varepsilon_{ini}/\varepsilon_0$) are given. For homogenous models, the first microcrack initiation occurred again early on and the subsequent microcrack area growth rate is high instantaneously after crack initiation. For the anisotropic models, the first microcrack initiation is delayed relative to the isotropic cases. Subsequently, further microcrack area accumulation is slow and only later increases to the growth rates of the isotropic cases. The increases in microcrack area were driven by microcrack growth in the isotropic models. However, for the anisotropic models, the microcrack area increases through both the formation of additional microcracks and the growth of individual microcracks, Fig. 7B. While the energy dissipation per total microcrack area was higher for the anisotropic models than for the isotropic models, Fig. 7C. Combining data from Fig. 7B and C, the energy dissipation per microcrack can be estimated. In the AnisoHmg model the energy dissipated per microcrack was approximately 1.5 times higher than in the AnisoHtg model while the difference for isotropic models was not substantial.

Fig. 8 depicts the spatial distribution of microcrack lengths (numbered from largest to smallest) at a total microcrack area of approximately 2.5×10^{-3} mm^2 in all models. The microcrack dis-

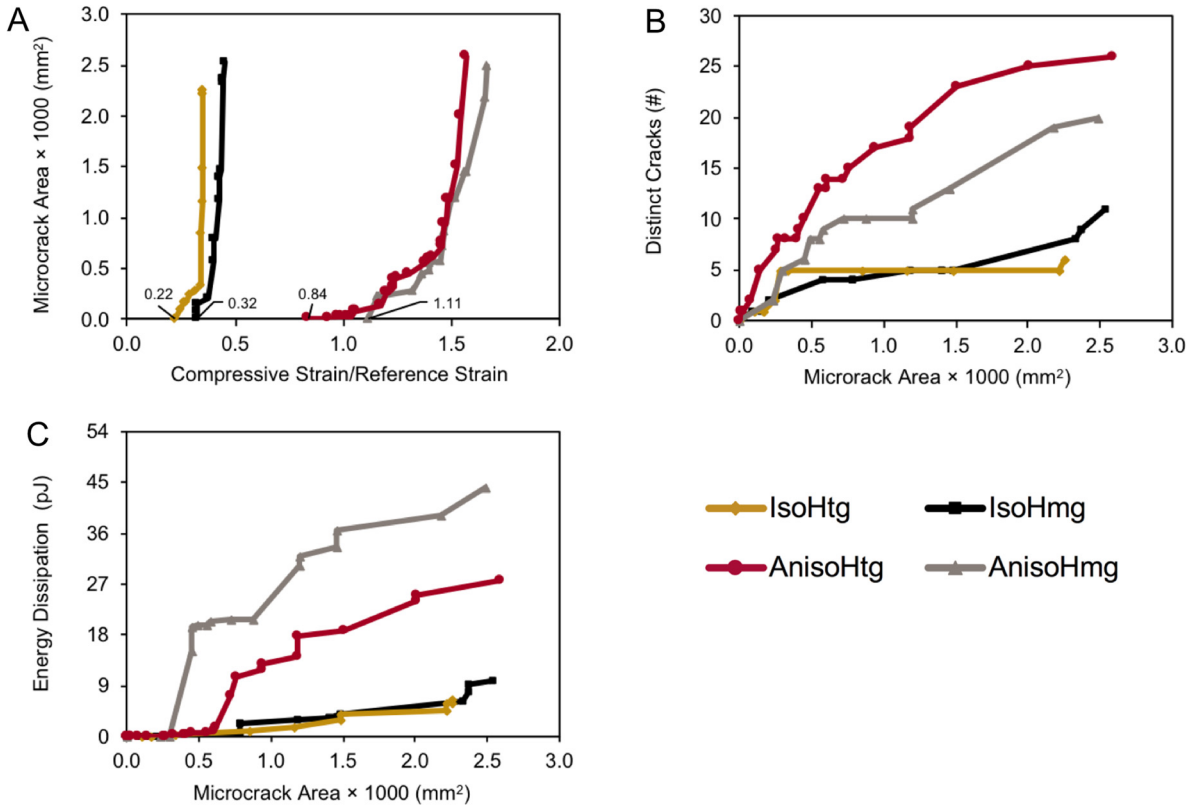

Fig. 7. Total microcrack characteristics in the bone core models: (A) Microcrack area vs. normalized applied strain (strain values at initiation provided): Anisotropy increased microcrack initiation strain and delayed microcrack growth, but heterogeneity reduced microcrack initiation strain; (B) Microcrack area vs. number of cracks: Increases in microcrack area were driven mainly by the growth of existing microcracks in the isotropic models and by the initiation of new microcracks in the anisotropic models: (C) Microcrack area vs. energy dissipation: Anisotropy substantially increased the energy dissipated per microcrack area with the effect being largest for the homogenous case.

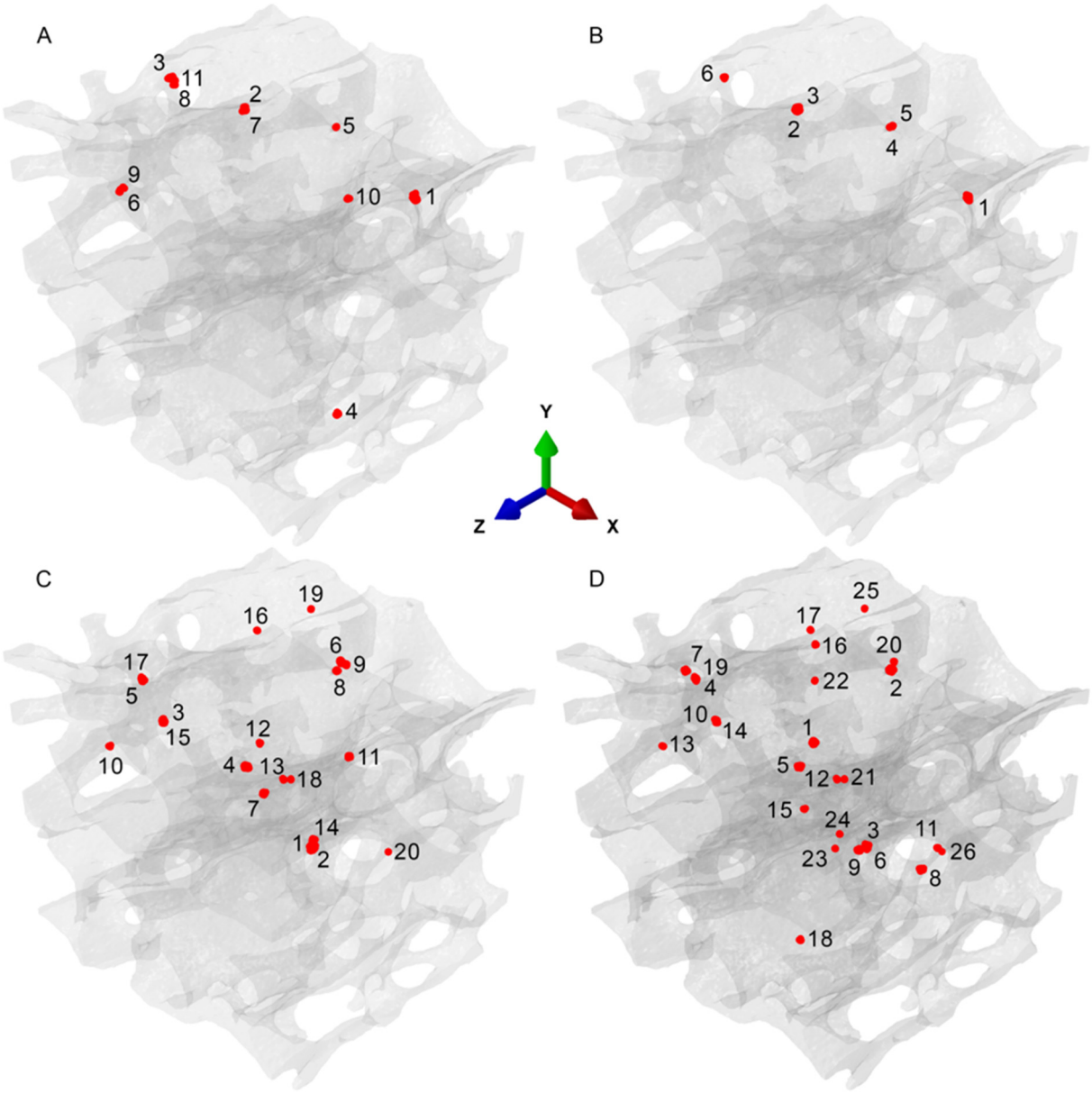

Fig. 8. Location of microcracks (labeled dots) at a total microcrack area of approximately 2.5×10^{-3} mm^2 numbered in order from largest to smallest microcrack in the (A) IsoHmg, (B) IsoHtg, (C) AnisoHmg and (D) AnisoHtg models demonstrated anisotropy alters microcrack locations and heterogeneity alters microcrack area distributions. Transaxial loading direction equals the z-axis.

tribution is dilute with cracks well separated from each other. Comparing predictions for the isotropic and anisotropic models, anisotropy drastically altered the location of microcracks and increased number of microcracks present. Heterogeneity altered the relative sizes of each microcrack within a model, but overall if a microcrack was present in a location in the homogeneous model a corresponding microcrack was also present in the heterogeneous model in both the isotropic and anisotropic case. Heterogeneity did not alter the location of the initial microcrack in the isotropic model, but did in the anisotropic model. For anisotropic models, several locations had multiple discrete and small microcracks in close proximity and this effect was more pronounced in the heterogeneous anisotropic model.

Fig. 9 summarizes the growth for individual microcracks with respect to the normalized post-initiation strain $(\varepsilon_{appl} - \varepsilon_{ini})/\varepsilon_0$. For the isotropic models with the maximum principal stress criterion, the growth of the initial transverse microcrack dominates over all other microcracks formed at a later stage. Although secondary microcracks formed, these remained comparatively small. This dominating effect was found to be most apparent in the isotropic homogeneous case. For anisotropic models, the initial microcrack did not become dominant. Several microcracks formed at a later time are of similar length (AnisoHmg) or even longer (AnisoHtg) than the initial microcrack. In addition several smaller microcracks formed.

4. Discussion

The present computation supported the hypothesis that microcracking is related to the biomechanical tissue anisotropy (i.e. transverse isotropic moduli and microcrack initiation criterion imposed on tissue anisotropy) and heterogeneity (i.e. spatially varying moduli and microcrack initiation strength). The hypothesis

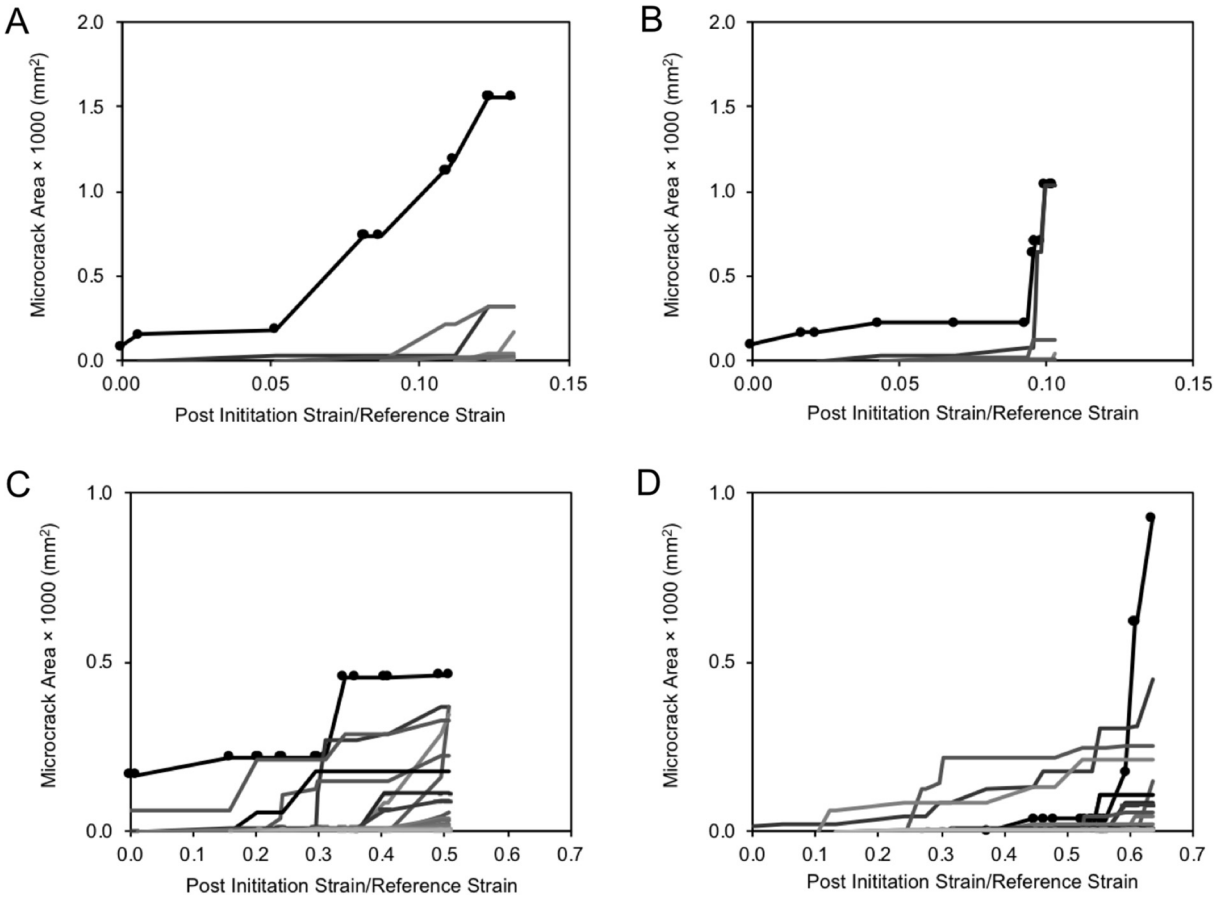

Fig. 9. Individual microcrack growth curves for the (A) IsoHmg, (B) IsoHtg, (C) AnisoHmg and (D) AnisoHtg models demonstrated that while for all models the total microcrack area was driven by a small fraction of the total microcrack number the initial crack dominated the isotropic models. The initial microcrack is denoted by lines with markers and the darker the line the earlier the crack initiated.

of the role of anisotropy was confirmed: only the models with anisotropy accounted for in the microcrack initiation criterion predicted the formation of linear microcracks, Figs. 4C-D, 5B, as well as a wide spatial distribution of similar-sized microcracks, Fig. 8C-D. Heterogeneity in the tissue was observed to locate microcracks closer to the experimentally observed locations near and parallel to the trabecular surface.

The deformation of trabeculae in a bone core involves complex stress states. Microcrack initiation in trabecular bone can be discussed in the context of the mechanics of axial deformation, bending and shear deformation, as well as torsion of individual trabecula. The mechanics of such stress and deformation problems on basic geometries (circular rods) is well understood. However, the specifics of the biomechanical properties of the trabecular bone tissue and the microarchitecture impose substantive complexities. Trabeculae are curved members with near circular cross section of varying diameter across the span, possessing radially graded mechanical properties as well as radial anisotropy. Structural members with low modulus at the surface and higher modulus in the interior can possess flexural stress distributions where the maximum normal stress no longer occurs at the surface (Aldousari, 2017). This effect has been described as a shielding effect in bone (Torres et al., 2016). Tissue heterogeneity is responsible for the alteration of initiation site for linear microcrack initiation. Then the question arises whether the initiation of linear microcracks is due to shear tractions or transversal normal tractions. Additional numerical experiments on the single trabeculae model, with either shear or normal separation blocked, reveal linear microcrack initiation as transverse shear dominated. In homogeneous and isotropic beams the maximum shear stress arises at the neutral axis. It is intrinsically connected to the linear dependence of the flexural stress in dependence on the distance from the neutral axis. This is similar to the anisotropic-homogenous case considered. The tissue heterogeneity alters the flexural stress state (Aldousari, 2017) such that a local maximum in flexural stresses occurs subsurface. That local maximum is then linked to secondary maximum in transverse shear stress near the surface. As the shear strength is low due to the tissue heterogeneity, linear microcrack initiation is predicted in the trabecular interior close to the trabecular surface. The radial symmetry of anisotropy and heterogeneity are responsible for the microcrack growth into internal microcracks with surfaces parallel to the trabecular surfaces. For the isolated trabeculae, this effect was not effective in delaying microcrack initiation, Fig. 5A. Heterogeneity did, however, increase the energy dissipation during microcrack growth in both the transverse and the linear microcracks, Fig. 6B, in the single trabeculae model. No conclusive evidence of similar effects on the bone core model could be established. Heterogeneity increased the number of microcracks (AnisoHm vs. AnisoHtg. Fig. 7B), but the respective energy dissipation was higher for the AnisoHmg case. Microcrack evolution in the single trabeculae model and the core model show similar trends in terms of microcrack area evolution in that anisotropy delays crack initiation and reduces microcrack area accumulation rate, Fig. 6A and A. In the single trabeculae model, however, all damage is due to a single defect, while in the core model multiple microcracks occur, Fig. 7B. The energy dissipation in the core, Fig. 7C, is thus a cumulated measure over all microcracks while in the single trabeculae this measure only accounts for a single

microcrack, Fig. 6B. Transverse microcracks were found to initiate from the trabecular surface and thus are always associated with the location of maximum strain. For linear microcracks the spatial association with the location of maximum strains depends on the tissue heterogeneity. If a trabeculae is homogeneous in elastic properties the microcrack location is not associated with the maximum strain. However, if the tissue elastic properties are heterogeneous, microcrack location and maximum strain location are closely associated. This explains the experimental findings of microcrack-strain association measured in (Goff et al. 2015a, b).

The present model approach can be useful in studies of the effects of various osteoporosis treatments on bone microcrack evolution (Allen and Burr, 2007). This can be accomplished by treatment related parametric modifications of model input parameters. Furthermore, the model can also be used in studies of biomedical devices such as bone screws. Thereby, this present approach would augment prior demonstrated approaches (Wirth et al., 2012) with information in local damage evolution."

Recent nanopillar compression experiments (Luczynski et al., 2015; Schwiedrzik et al., 2017) have demonstrated modulus to strength ratios in the range of 50–100. Considering that these values where obtained on nanopillars which often exhibit size dependent strengthening and the use of a 0.4% off set criterion for the strength, it is reasoned that the modulus to strength ratio of 500 provides a reasonable bound value. The tissue anisotropy was transversely isotropic but no principle barrier exists to a fully orthotropic extension of the model. Microcrack formation was predicted by either the maximum principal stress or the maximum nominal stress criterion. A model where the two criteria compete could further elucidate the microcrack formation process and the competition between linear and transverse microcracks. However, as linear microcracking is a major morphology, the maximum nominal stress criterion in conjunction with the transversely isotropic orientation distribution appears as a viable choice. A further challenge for future work is to extend the model to account explicitly for plasticity-like irreversible deformation processes (Gupta et al., 2007; Fritsch et al., 2009; Luczynski et al., 2015). Then, the dissipative terms would no longer be lumped into the cohesive zone model but separated into volumetric and surface terms.

5. Conclusion

The present study demonstrated that trabecular tissue anisotropy—reflected in the spatial distribution of the tissue elastic response, the anisotropy of the elastic properties and the directional maximum nominal stress microcrack initiation criterion—plays an important role in the formation of linear microcracks in trabecular bone. Only if all such features are accounted for in a model of microcrack formation, is it possible to predict the shape and distributed microcracking typically observed in trabecular bone.

Acknowledgements

This material was based upon work supported by the National Science Foundation under Grant No. 1643164. This work used the Extreme Science and Engineering Discovery Environment (XSEDE), which is supported by National Science Foundation grant number ACI-1548562. Carmen Herrera contribution to the 3D images of microcracks is acknowledged.

Conflict of interest statement

The authors declare that no conflict of interests exist.

References

Abdel-Wahab, A.A., Maligno, A.R., Silberschmidt, V.V., 2012. Micro-scale modelling of bovine cortical bone fracture: analysis of crack propagation and microstructure using X-FEM. Comp. Mat. Sci. 52, 128–135.
Acevedo, C., Stadelmann, V.A., Pioletti, D.P., Alliston, T., Ritchie, R.O., 2018. Fatigue as the missing link between bone fragility and fracture. Nat. Biomed. Eng. 1.
Aldousari, S.M., 2017. Bending analysis of different material distributions of functionally graded beam. Appl. Phys. A 123, 296.
Allen, M.R., Burr, D.B., 2007. Three years of alendronate treatment results in similar levels of vertebral microdamage as after one year of treatment. J. Bone Mineral Res. 22, 1759–1765.
Besdo, S., Vashishth, D., 2012. Extended Finite Element models of introcortical porosity and heterogeneity in cortical bone. Comp. Mat. Sci. 64, 301–305.
Elices, M.G.G.V., Guinea, G.V., Gomez, J., Planas, J., 2002. The cohesive zone model: advantages, limitations and challenges. Eng. Fract. Mech. 69, 137–163.
Feerick, E.M., Liu, X.C., McGarry, P., 2013. Anisotropic mode-dependent damage of cortical bone using the extended finite element method (XFEM). J. Mech. Behav. Biomed. Mater. 20, 77–89.
Fritsch, A., Hellmich, C., Dormieux, L., 2009. Ductile sliding between mineral crystals followed by rupture of collagen crosslinks: experimentally supported micromechanical explanation of bone strength. J. Theor. Bio. 260, 230–252.
Frost, H.M., 1960. Presence of microscopic cracks in vivo in bone. Henry Ford Hosp. Med. Bull. 8, 25–35.
Georgiadis, M., Guizar-Sicairos, M., Gschwend, O., Hangartner, P., Bunk, O., Müller, R., Schneider, P., 2016. Ultrastructure organization of human trabeculae assessed by 3D sSAXS and relation to bone microarchitecture. PLOS ONE 11 (e0159), 838.
Goff, M.G., Lambers, F.M., Nguyen, T.M., Sung, J., Rimnac, C.M., Hernandez, C.J., 2015a. Fatigue-induced microdamage in cancellous bone occurs distant from resorption cavities and trabecular surfaces. Bone 79, 8–14.
Goff, M.G., Lambers, F.M., Sorna, R.M., Keaveny, T.M., Hernandez, C.J., 2015b. Finite element models predict the location of microdamage in cancellous bone following uniaxial loading. J. Biomech. 48, 4142–4148.
Gupta, H.S., Fratzl, P., Kerschnitzki, M., Benecke, G., Wagermaier, W., Kirchner, H.O., 2007. Evidence for an elementary process in bone plasticity with an activation enthalpy of 1 eV. J. Roy. Soc. Int. 4, 277–282.
Hamed, E., Jasiuk, I., 2013. Multiscale damage and strength of lamellar bone modeled by cohesive finite elements. J. Mech. Behav. Biomed. Mat. 28, 94–110.
Hammond, M.A., Wallace, J.M., Allen, M.R., Siegmund, T., 2018. Incorporating tissue anisotropy and heterogeneity in finite element models of trabecular bone altered predicted local stress distributions. Biomech. Model Mechanobio. 17, 605–614.
Lambers, F.M., Bouman, A.R., Rimnac, C.M., Hernandez, C.J., 2013. Microdamage caused by fatigue loading in human cancellous bone: relationship to reductions in bone biomechanical performance. PLoS One 8, e83662.
Larrue, A., Rattner, A., Peter, Z.A., Olivier, C., Laroche, N., Vico, L., Peyrin, F., 2011. Synchrotron radiation micro-CT at the micrometer scale for the analysis of the three-dimensional morphology of microcracks in human trabecular bone. PLoS One 6, e21297.
Lu, T.J., Xia, Z.C., Hutchinson, J.W., 1994. Delamination of beams under transverse shear and bending. Mater. Sci. Eng. A 188, 103–112.
Luczynski, K.W., Steiger-Thirsfeld, A., Bernardi, J., Eberhardsteiner, J., Hellmich, C., 2015. Extracellular bone matrix exhibits hardening elastoplasticity and more than double cortical strength: evidence from homogeneous compression of non-tapered single micron-sized pillars welded to a rigid substrate. J. Mech. Behav. Biomed. Mater. 52, 51–62.
Launey, M.E., Buehler, M.J., Ritchie, R.O., 2010. On the mechanistic origins of toughness in bone. Annu. Rev. Mat. Res. 40, 25–53.
Mori, S., Harruff, R., Ambrosius, W., Burr, D.B., 1997. Trabecular bone volume and microdamage accumulation in the femoral heads of women with and without femoral neck fractures. Bone 21, 521–526.
Reisinger, A.G., Pahr, D.H., Zysset, P.K., 2011. Principal stiffness orientation and degree of anisotropy of human osteons based on nanoindentation in three distinct planes. J. Mech. Behav. Biomed. Mat. 4, 2113–2127.
Reznikov, N., Chase, H., Brumfeld, V., Shahar, R., Weiner, S., 2015. The 3D structure of the collagen fibril network in human trabecular bone: relation to trabecular organization. Bone 71, 189–195.
Rho, J.Y., Hobatho, M.C., Ashman, R.B., 1995. Relations of mechanical properties to density and CT numbers in human bone. Med. Eng. Phys. 17, 347–355.
Ridha, H., Thurner, P.J., 2013. Finite element prediction with experimental validation of damage distribution in single trabeculae during three-point bending tests. J. Mech. Behav. Biomed. Mat. 27, 94–106.
Ritchie, R.O., 2010. How does human bone resist fracture? Ann. NY Acad. Sci. 2010 (1192), 72–80.
Schwiedrzik, J., Taylor, A., Casari, D., Wolfram, U., Zysset, P., Michler, J., 2017. Nanoscale deformation mechanisms and yield properties of hydrated bone extracellular matrix. Acta Biomat. 60, 302–314.
Siegmund, T., Allen, M.R., Burr, D.B., 2008. Failure of mineralized collagen fibrils: modeling the role of collagen cross-linking. J. Biomech. 41, 1427–1435.
Sukumar, N., Dolbow, J.E., Moës, N., 2015. Extended finite element method in computational fracture mechanics: a retrospective examination. Int. J. Fract. 196, 189–206.
Tassani, S., Pani, M., Noailly, J., Gonzalez Ballester, M.A., 2018. Trabecular fracture zone might not be the higher strain region of the trabecular framework. Front. Mat. 5, 6.

Thurner, P.J., Erickson, B., Jungmann, R., Schriock, Z., Weaver, J.C., Fantner, G.E., Schitter, G., Morse, D.E., Hansma, P.K., 2007. High-speed photography of compressed human trabecular bone correlates whitening to microscopic damage. Eng. Fract. Mech. 74, 1928–1941.

Tomar, V., 2008. Modeling of dynamic fracture and damage in two-dimensional trabecular bone microstructures using the cohesive finite element method. J. Biomech. Eng. 130, 021021.

Torres, A.M., Matheny, J.B., Keaveny, T.M., Taylor, D., Rimnac, C.M., Hernandez, C.J., 2016. Material heterogeneity in cancellous bone promotes deformation recovery after mechanical failure. Proc. Nat. Acad. Sci. 113, 2892–2897.

Verborgt, O., Gibson, G.J., Schaffler, M.B., 2000. Loss of osteocyte integrity in association with microdamage and bone remodeling after fatigue in vivo. J. Bone Miner. Res. 15, 60–67.

Wang, X., Masse, D.B., Leng, H., Hess, K.P., Ross, R.D., Roeder, R.K., Niebur, G.L., 2007. Detection of trabecular bone microdamage by micro-computed tomography. J. Biomech. 40, 3397–3403.

Wenzel, T.E., Schaffler, M.B., Fyhrie, D.P., 1996. In vivo trabecular microcracks in human vertebral bone. Bone 19, 89–95.

Wirth, A.J., Müller, R., van Lenthe, G.H., 2012. The discrete nature of trabecular bone microarchitecture affects implant stability. J. Biomech. 45, 1060–1067.

Yeni, Y.N., Fyhrie, D.P., 2003. A rate-dependent microcrack-bridging model that can explain the strain rate dependency of cortical bone apparent yield strength. J. Biomech. 36, 1343–1353.